ADVANCES IN ATMOSPHERIC SCIENCES, VOL. 39, DECEMBER 2022, 2008–2023

• **Original Paper** •

Characteristics of Pre-summer Daytime Cloud Regimes over Coastal South China from the Himawari-8 Satellite※

Mingxin LI[1], Yali LUO[*1,2], and Min MIN[3]

[1]*State Key Laboratory of Severe Weather*, *Chinese Academy of Meteorological Sciences*, *Beijing* 100081, *China*

[2]*Collaborative Innovation Center on Forecast and Evaluation of Meteorological Disasters*, *Nanjing University of Information Science and Technology*, *Nanjing* 210044, *China*

[3]*School of Atmospheric Sciences*, *and Guangdong Province Key Laboratory for Climate Change and Natural Disaster Studies*, *Sun Yat-sen University*, *Guangzhou* 519082, *China*

(Received 17 April 2021; revised 24 August 2021; accepted 30 August 2021)

ABSTRACT

Using the high spatiotemporal resolution (2 km-and-10 min) data from the Advanced Himawari Imager onboard the Himawari-8 satellite, this study documents the fine-scale characteristics of daytime cloud regimes (CRs) over coastal South China during the pre-summer rainy season (April–June). Six CRs (CR1–CR6) are identified based on the joint frequency distribution of cloud top brightness temperature and cloud optical thickness, namely, the optically thin-to-moderate cloud mixture, optically thin warm clouds with cirrus, optically thick warm clouds, weak convective cloud mixture, strong convective clouds, and extreme, deep convective clouds. The optically thick warm clouds are the major CR during April and May, with higher frequencies over land, especially along the urban agglomeration, rather than the offshore which may be an indicator of the higher aerosol concentrations being a contributing factor over the cities. The CRs with weak convective cloud mixtures and strong convective clouds appear more frequently over the land, while the two CRs with optically thinner clouds occur mainly offshore.

Synoptic flow patterns (SPs) are objectively identified and examined focusing on those favoring the two major rain-producing CRs (CR5 and CR6) and the highly reflective CR with optically thick warm clouds (CR3). The two SPs favoring CR5 and CR6 are characterized by abundant moisture with low-level jets after monsoon onset, and a northwest high-southeast low pattern with strong dynamic convergence along the coastline, respectively. The non-convective CR3 with high reflectance is related to a SP that features the western North Pacific subtropical high extending more westward, leading to a moderate moisture supply and a wide range of convective available potential energy, but also, large convective inhibition.

Key words: cloud regime, monsoon onset, synoptic pattern, satellite data, spatiotemporal distribution

Citation: Li, M. X., Y. L. Luo, and M. Min, 2022: Characteristics of pre-summer daytime cloud regimes over coastal South China from the Himawari-8 satellite. *Adv. Atmos. Sci.*, **39**(12), 2008–2023, https://doi.org/10.1007/s00376-021-1148-1.

Article Highlights:

- Six CRs over Coastal South China are identified with the 2 km-and-10 min resolution data from Himawari-8
- The occurrence frequency of the CRs contrast remarkably prior and after the SCS monsoon onset and between the land and nearby offshore
- The three high-impact CRs are closely related to distinctive synoptic patterns

1. Introduction

Clouds play a vital role in the earth's climate system as they can greatly modify the earth energy balance by scattering/absorbing shortwave radiation and absorbing/emitting longwave radiation (Trenberth et al., 2009; Stephens et al., 2012), and govern the response of the global-scale hydrological cycle to climate forcing (Stephens, 2005). As traditional cloud types rarely occur in isolation over a large area, a description in terms of the dominant mixture of cloud types is more fitting in a variety of contexts (Oreopoulos et al., 2016). Numerous studies have been carried out to document

※ This paper is a contribution to the special issue on Cloud–Aerosol–Radiation–Precipitation Interaction: Progress and Challenges.

* Corresponding author: Yali LUO
Email: ylluo@cma.gov.cn

the properties of cloud regimes (CRs) throughout the world. The CRs are identified based on observed cloud information and can then be linked to atmospheric characteristics (Zhang et al., 2007), which provide a possibility for studying cloud characteristics in a simplified framework (Jakob and Schumacher, 2008). Usually, the cloud top pressure or temperature representing the cloud height information, and the cloud optical thickness yields information about the cloud physical depth and population/size of hydrometeor particles that are used jointly for CR identification. While most of the studies analyzed CRs on a global scale (Oreopoulos et al., 2014, 2016; Leinonen et al., 2016) or over the tropics (Jakob and Tselioudis, 2003; Rossow et al., 2005; Zhang et al., 2007; Jakob and Schumacher, 2008; Tan et al., 2013), a few focused on higher latitudes (Gordon et al., 2005). A recent study by Wu and Chen (2021) investigated the regional differences in CRs between northern India and Southeast China. Among the abovementioned studies, very few investigated the synoptic conditions and meteorological parameters associated with CRs.

The pre-summer rainy season (April–June) accounts for about a half of the annual precipitation amount over South China with the rainfall reaching its peak after the onset of the South China Sea (SCS) monsoon in mid-to-late May (Ding, 1994; Luo et al., 2017). As most precipitation during the pre-summer season over South China is produced by mesoscale convective systems (MCSs) (Luo et al., 2013, 2020), previous studies mainly focused on the heavy rainfall-producing storms. While some studies explored physical mechanisms governing the initiation and evolution of convective storms and heavy rainfall production through numerical modeling (e.g., Du and Chen, 2019; Yin et al., 2020), numerous studies conducted an observational analysis to document the rainfall characteristics and convective processes. Most of the observational analyses used observations from surface automatic weather stations (AWSs) (Wang et al., 2014; Wu et al., 2019) and ground-based Doppler radars (Chen et al., 2014; Li et al., 2021). A few satellite products, such as those from the Tropical Rainfall Measuring Mission (TRMM) (Kummerow et al., 1998) and CloudSat/Cloud-Aerosol Lidar and Infrared Pathfinder Satellite Observations (CALIPSO) (Stephens et al., 2002), are used to depict convective properties of the monsoon precipitation systems over South China (e.g., Xu et al., 2009; Luo et al., 2013).

The underlying surface of coastal South China is very complex. An extensive urban agglomeration is situated in Guangdong province as a result of the rapid urbanization that has occurred during the past three decades. South China is adjacent to the northern SCS to the southeast and surrounded by mountains on the other sides (Fig. 1a). The thermal and dynamic effects of topography, urban, and land-sea contrasts could exert profound impacts on clouds and precipitation, as found over other places of the world (e.g., Huff and Vogel, 1978; Whiteman, 2000). Meanwhile, levels of anthropogenic aerosols are higher over the urban agglomeration than its surroundings, especially than that of the SCS, as suggested by larger aerosol optical depth over the cities (de Leeuw et al., 2018). The more abundant aerosols could significantly reduce MCS occurrences over Southern China, in April, leading to less rainfall (Zhang et al., 2020), not only due to the direct radiative scattering of aerosols and the indirect enhancement of non-MCS liquid cloud reflectance by aerosols via "Twomey effects" (Twomey, 1977) which serves to stabilize the regional atmosphere but also because of the microphysical and dynamical responses of the MCS to aerosols. Moreover, the onset of the SCS monsoon leads to substantial changes in the pathways and sources of moisture for South China rainfall (Chen, 2018) and in the thermodynamic and dynamic conditions under which rainstorms form over South China during the pre-summer season (Luo et al., 2013; Li et al., 2020).

The abovementioned meteorological and environmental

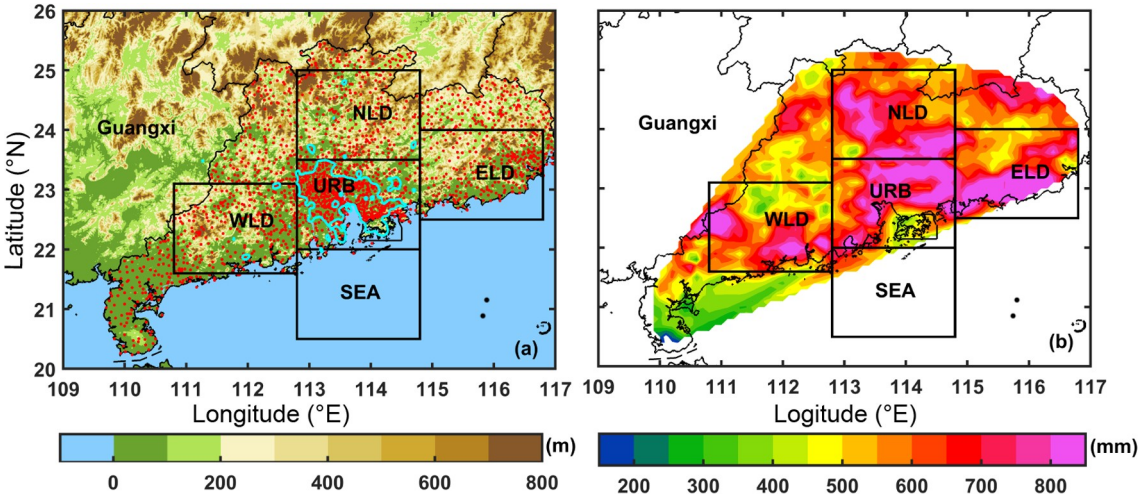

Fig. 1. (a) Topography over South China (shading) with the five subregions (black boxes) of the targeted area in this study. Red dots represent the location of the automatic weather stations over Guangdong province. The cyan line outlines the area with high-density nighttime lights. (b) Distribution of the daytime (0800–1700 LST) rainfall accumulation (mm) over Guangdong province from April to June of 2016–17.

factors are expected to influence the properties and spatiotemporal distribution of clouds over this monsoon coastal region both before and after SCS monsoon onset. In addition to the amount and distribution of rainfall that is closely related to the MCSs, the local climate can also be affected by a variety of clouds that form under different synoptic conditions. Cloud regime (CR) studies are capable of presenting a more complete picture of the cloud characteristics. However, most CR studies have focused on broader areas with coarse-resolution data due to observation limitations. The precipitation estimation from the TRMM is usually used to match the CRs. Thus, it is difficult to determine the local regional variations of CRs and their fine-scale surface rainfall characteristics. Moreover, few CR studies have examined their associated synoptic patterns, and little is known about CRs over South China.

Built upon previous studies, this study investigates CR properties over South China during the pre-summer season using the cloud products with high spatiotemporal resolutions (2 km and 10 min) based on the Advanced Himawari Imager (AHI) onboard the Himawari-8 satellite. Both the cloud optical properties and the vertical extension of clouds are considered in the CR classification. The occurrence frequency, microphysical properties, and rainfall production of these CRs are comparatively analyzed among five subregions in the targeted area (Fig. 1a). Among the classified CRs, the major rain-producing CRs and the CR with both high reflectance and high occurrence frequency are further examined in terms of synoptic background favoring their formation.

The remainder of this paper is organized as follows: The dataset and methodology are introduced in section 2. The main results concerning the properties of the CRs, their related synoptic flow patterns (SPs), and their associated environmental thermodynamic and dynamic parameters are presented in section 3. Section 4 provides a summary and conclusions.

2. Data and Methods

2.1. *The study area and five subregions*

The targeted area of this study mainly covers the Guangdong province in coastal South China and the adjacent northern SCS (Fig. 1a), which is divided into five 1.5° × 2° subregions based upon its underlying surface features. The west land region (WLD) contains the mountains and coastal area in southwestern Guangdong. The north land region (NLD) is mainly occupied by the inland mountains. The urban region (URB) is dominated by cities, which can be seen from the Defense Meteorological Satellite Program's Operational Linescan System (DMSP/OLS) high-density nighttime lights. SEA is the offshore area south of URB. The east land region (ELD) mainly includes the coastal mountains and a small fraction of water. The gauge-based daytime rainfall accumulation (Fig. 1b) during the April to June periods of 2016–17 exhibits several rainfall centers over the western and northern mountains, the urban region, and the coastal area in ELD, respectively, which are well covered by the subregions. Note that daytime, i.e., 0800–1700 local solar time (LST; LST = UTC + 8 h) rainfall is used here to be consistent with the daytime satellite observation utilized, which is described in detail below.

2.2. *TBB data and cloud products*

This study, following previous studies, utilizes the joint frequency distribution of the brightness temperature (TBB) and cloud optical thickness (COT) within each of the subregions to define a CR. The cloud products are available every 10 min and 2 km at nadir, from April to June of the years 2016–17 based on the AHI onboard the Himawari-8 geostationary satellite. The Himawari-8 satellite was launched by the Japan Meteorological Agency on 7 October 2014 and has been operating at 140.7°E longitude since July 2015. The AHI has 16 bands ranging from 0.47 μm to 13.3 μm with a spatial resolution from 0.5 km to 2 km. Full disk images are taken every 10 min (Bessho et al., 2016). The TBB data is obtained from the 10.4 μm infrared channel provided by the AHI. The cloud mask, COT, and cloud phase products are retrieved from the Himawari-8 observations using the Fengyun Geostationary Algorithm Testbed-Imager (FYGAT-I) science product algorithm (Min et al., 2017). The cloud mask product has been validated and used by several studies (Chen et al., 2019; Wang et al., 2019). The cloud phase is identified by the classical cloud emissivity algorithm (Pavolonis et al., 2005). The COT product is retrieved with a Daytime Cloud Optical and Microphysical Property (DCOMP) algorithm based on the 0.64 μm and 2.25 μm bands and a one-dimensional variational algorithm (Walther et al., 2011; Min et al., 2017). Thus, only daytime (i.e., the zenith angle is smaller than 65°) cloud regimes (CRs) are analyzed in this study. During the 2016–17 pre-summer season, the abovementioned satellite datasets are valid for 87.6% of the daytime period. If a subregion contains less than 25 cloudy pixels (i.e., cloud fraction less than about 0.4% in the subregion) at a time, it is defined as clear-sky. If the number of pixels with COT missing is divided by the total number of cloudy pixels over a subregion at a given time is larger than 20%, it is considered as missing data. Both the clear-sky and missing data are excluded from further analysis for this subregion.

2.3. *Surface rainfall dataset and ERA5 reanalysis*

The 10-min rainfall data collected at 2418 AWSs in Guangdong (Fig. 1a) are used to describe the surface rainfall produced by each CR. The 10-min rainfall records are gridded with a horizontal grid spacing of 0.1°. The fifth generation of the European Centre for Medium-Range Weather Forecasts (ECMWF) provided the atmospheric reanalysis of the global climate (ERA5) dataset, with 0.25° horizontal resolution, that was used to examine the SPs which influenced the identified CRs during the study period.

2.4. *Classification of cloud regimes and synoptic patterns*

The cloud top TBB and COT within a subregion jointly define a cloud element. The cluster analysis is performed over the mesoscale 1.5° (lat) × 2° (lon) subregions with the cloud elements. A total of 33 772 cloud elements were found during the analysis period. These cloud elements are clustered into six groups (i.e., CRs) with the K-means algorithm (Anderberg, 1973), which has been previously applied to cluster analyses of tropical clouds (Jakob and Tselioudis, 2003; Zhang et al., 2007, Tan et al., 2013) and clouds over the southern Great Plains of the US (Gordon et al., 2005). Specifically, four clusters are first classified using the K-means algorithm based on the joint frequency distributions of the cloud top TBB and the COT. With more than 45% of the cloud elements being classified into one big group, these elements are further clustered into three new groups (i.e., CR4 to CR6). A detailed description outlining the CR identification is provided in the electronic supplementary materials (ESM).

To examine the synoptic background under which the CRs take place, the obliquely rotated T-mode principal component technique (PCT; Huth, 1993) is used. This method has been widely used in studies on synoptic patterns (e.g., Zhang et al., 2012; Li et al., 2016). In the present work, the daily 925 hPa geopotential height (GPH) at 12 LST, from the ERA5 reanalysis, during the study period within the domain of 15°N–30°N and 105°E–125°E, are classified into nine patterns using the PCT. Nine patterns are chosen following previous studies that utilized the PCT method (e.g., Zhang et al., 2012; Zhao et al., 2013; He et al., 2017). The temperature, humidity, horizontal wind, and vertical velocity are utilized to examine larger-scale features around the targeted area under the synoptic patterns (SPs). Selected parameters such as the convective available potential energy (CAPE) of the most unstable parcel, convection inhibition (CIN), and total precipitable water (PW) over the targeted area are also calculated with the ERA5.

3. Results

3.1. *Cloud Regimes*

3.1.1. *Joint frequency distributions of cloud TBB and COT*

Figure 2 shows the joint frequency distributions of TBB and COT for the centroids of the six CRs obtained using the K-means method, with a bin width of 2 K and 2 for TBB and COT, respectively. Although the values of COT range from 0–150, occurrences of COT beyond 50 are included in the largest bin considered (i.e., COT of 48–50) in Fig. 2 for better illustration. Occurrence frequencies of CR1 to CR6 account for about 15.3%, 6.2%, 25.5%, 16.7%, 31.7%, and 4.6% of the total cloud elements, respectively. With high frequencies located at COTs of 0–10 and TBBs of 295–265 K, CR1 mainly consists of optically thin-to-moderate clouds and is characterized by a mixture of shallow low clouds and a small fraction of cirrus. With a small number of cloud pixels located at COT of 50 and above, there also exists a small portion of thick ice clouds in CR1. Both CR2 and CR3 are dominated by low-top clouds warmer than about 280 K, with a small COT (mostly <10) in CR2 but, optically thicker clouds (such as nimbostratus, stratocumulus, and stratus) are much more common in CR3. Note that CR3 is one of the two most frequently occurring CRs among the six CRs (the other is CR5), which is consistent with Li et al. (2004) who showed that stratocumulus is the most common cloud type along the coastline of southeastern China during spring and summer. The clouds within CR1–CR3 can hardly produce intense rainfall, given the generally small COT of CR1 and CR2 and the low cloud-tops of CR2 and CR3. However, CR3, with its abundant optically thick clouds, is able to induce strong cooling effects by reflecting solar radiation energy and thus significantly influence the local climate (Poetzsch-Heffter et al., 1995).

The cloud regimes, CR4–CR6, consist of optically thick clouds with varying cloud-top heights around and above the melting level, suggesting different convective intensities associated with the cloud elements. In addition to a large fraction of warm, thick clouds, CR4 has a large number of thick clouds with lower TBB (about or <273 K) implying the existence of convective clouds. The thick clouds (COT > about 15) in both CR5 and CR6 extend to higher altitudes relative to CR4, with the TBB most frequently occurring at about 250–220 K and 220–200 K, respectively, suggesting abundant deep convective clouds. For CR4 to CR6, the TBB of the optically thickest cloud pixels tends to decrease and the area of optically thick clouds tends to increase, suggesting enhanced convective intensity. The abovementioned distinct features of the six CRs confirm that the classification results are reasonable.

3.1.2. *Cloud fraction and phases*

The fractional area occupied by cloudy pixels in each subregion at a certain time, i.e., cloud fraction, is a basic parameter of the CRs' macroscale characteristics. Statistics of cloud fractions for these CRs are shown by boxplots in Fig. 3a. The three CRs with convective signatures (CR4–CR6) have cloud fractions mostly close to one, suggesting that they occupy the entire subregion when present. The optically thick, lower-topped CR3 has cloud fractions ranging from about 0.6 to 1, with a median of 0.9. Cloud fractions of CR1 (mainly shallow warm clouds along with a small amount of cirrus) are comparable to those of CR3. The optically thin, warm clouds (CR2) have the smallest cloud fraction among the six CRs, ranging from 0.3 to 1 with a median of about 0.7.

The percentages of pixels of the five cloud phases (i.e., water, supercooled water, thick ice, cirrus, and overlapping clouds) within each cloud element are shown by boxplots for each CR in Figs. 3b–f. Note that the overlapping clouds are translucent ice clouds superimposed on lower opaque clouds. The two most common CRs (CR3 and CR5) consist

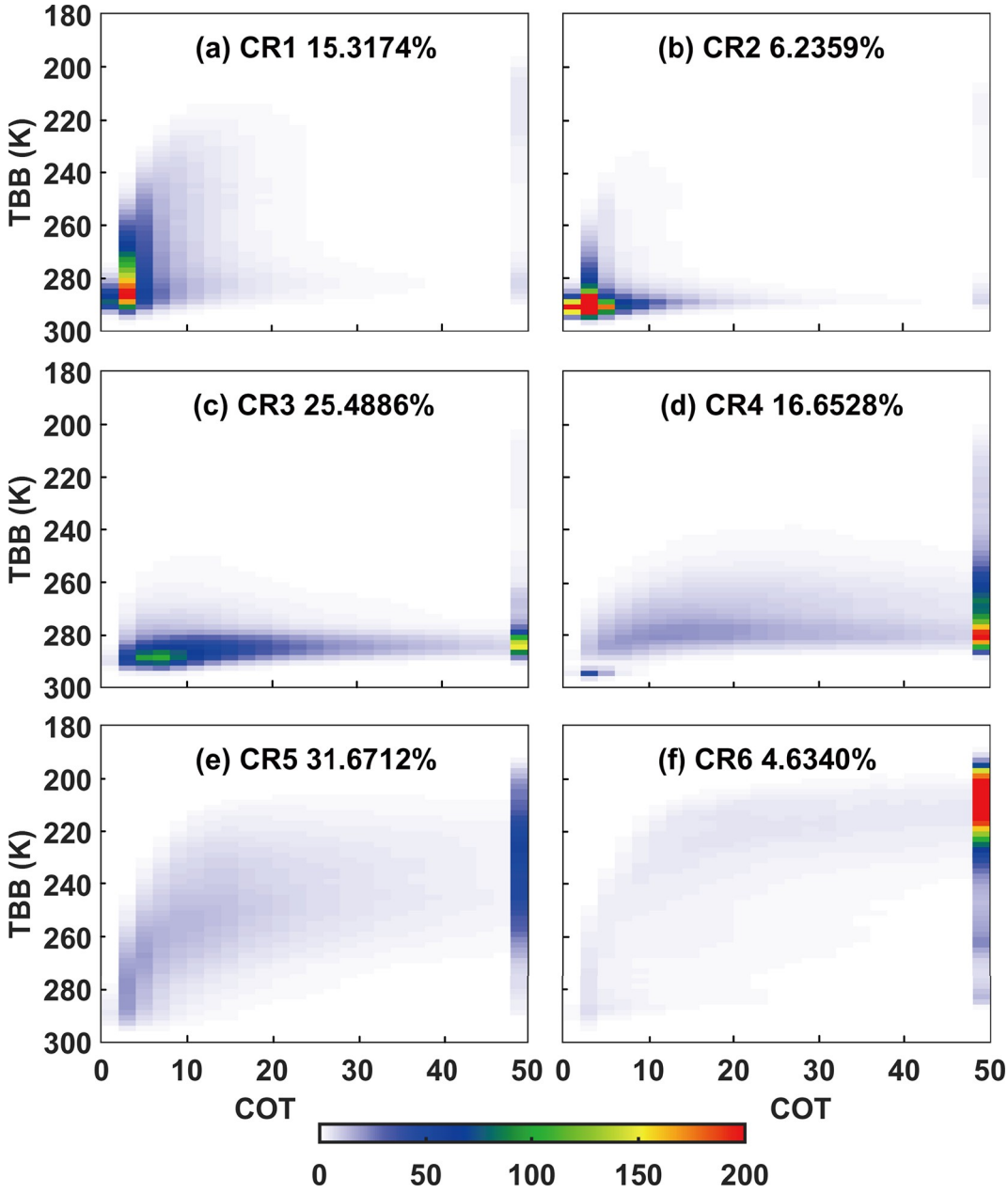

Fig. 2. The COT-TBB joint frequency distributions of the centroids of the six CRs. (a) CR1: optically thin mixture clouds. (b) CR2: optically thin warm clouds. (c) CR3: optically thick warm clouds. (d) CR4: weak convective clouds. (e) CR5: strong convective clouds. (f) CR6: extreme, deep convective clouds. The fractional contribution of each CR to the total frequency of CR1–CR6 is labeled in each panel.

mainly of water clouds and thick ice clouds (median percentages of 0.9 and 0.55), respectively, with CR5 also having a small portion of overlapping clouds (median percentage of 0.2). Cloud regime six (CR6) has even larger percentages of thick ice (median of 0.87) than CR5 with negligible water clouds, indicating that CR6 is almost completely composed of deep convective clouds (which is consistent with its concentrated frequency distribution with large COTs and low TBBs (Fig. 2f). Cloud regime four (CR4) consists of water clouds, overlapping clouds, supercooled water clouds, and thick ice clouds in descending order of the median percentages (0.43, 0.17, 0.07, and 0.04). Such complicated cloud structures of CR4 suggest multiple coexisting cloud types in different stages of evolving convective systems. The optically thin-to-moderate clouds of CR1 also possess multiple cloud phases but in a different order, i.e., cirrus, overlapping clouds, water clouds, and thick ice clouds (medians of 0.32, 0.26, 0.14, and 0.09, respectively). The remaining CR (i.e., CR2) mostly consists of water clouds and cirrus with median percentages of 0.46 and 0.32, respectively. The overall results about cloud phases associated with the CRs are consistent with the joint frequency distributions discussed in subsection 3.1.1. Based on these analysis results and for convenience, the six CRs (CR1 to CR6) are referred to, here-

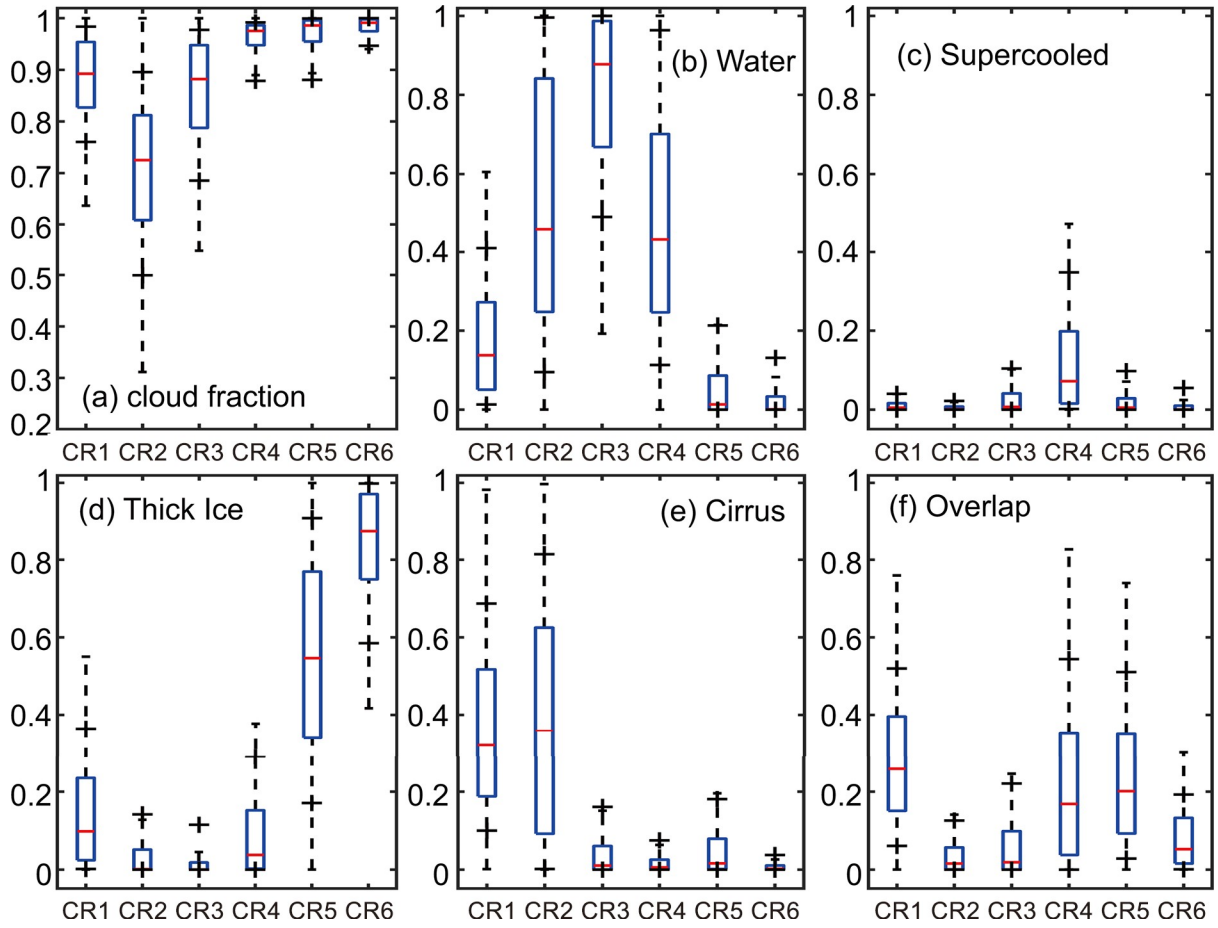

Fig. 3. Boxplots of (a) cloud fraction of the CRs and (b–f) percentage of the cloud phase pixels in the CRs, i.e., water, supercooled, thick ice, cirrus, overlap. Plus signs denote the 10th–90th percentiles, and blue boxes denote the 25th–75th percentiles, with the red horizontal bar at the median value. Vertical dashed lines (whiskers) extend to ± 2.7σ.

after, as optically thin-to-moderate cloud mixture, optically thin warm clouds with cirrus, optically thick warm clouds, weak convective cloud mixture, strong convective clouds, and extreme, deep convective clouds, respectively. Examples of these CRs, including the spatial distributions of TBBs and COTs at four selected times along with the synoptic flow pattern at the nearest time of the ERA5 before the four selected times, can be found in the ESM. Compared with the ISCCP (The International Satellite Cloud Climatology Project) CRs identified by Tan et al. (2013), the strong convective clouds, and extreme, deep convective clouds (CR5 and CR6) are similar to the regime CD (deep stratiform), while the weak convective cloud mixture (CR4) resembles regime CC (convective cirrus) in their study. The optically thin warm clouds with cirrus (CR2) and optically thick warm clouds (CR3) are probably included in the regime SS (Stratocumulus) in Tan et al. (2013). Moreover, they also have a mixture CR like the thin-to-moderate cloud mixture (CR1) in this study.

3.2. *Seasonal and regional variations of CRs*

Table 1 shows the occurrence frequency and the relative occurrence frequency (%) of each CR over the five subregions during April, May, and June, respectively. The daily mean occurrence frequency both before and after the SCS monsoon onset is also listed in Table 1. Here, the occurrence frequency of one CR is defined as the number of cloud elements that are classified to this CR. The relative occurrence frequency of each CR during each month is calculated as the occurrence frequency of the CR in the month divided by the total occurrence frequency of CR1–CR6 during the same month. The SCS monsoon onset takes place in the pentad of 16–20 May in 2016 and 2017, determined following the National Climate Center of China Meteorological Administration (http://cmdp.ncc-cma.net/Monitoring/monsoon.php) (Li et al., 2020). Therefore, the prior- and after-monsoon-onset periods cover 45 and 41 days yr^{-1}, respectively, excluding the monsoon-onset pentad. The total occurrence frequencies of the CRs are largely comparable among the three months (11060, 12084, 10628) differing, at most, by about 13.6%. However, those of each CR vary substantially month to month.

The optically thick warm clouds (CR3) mostly occur prior to the SCS monsoon onset, with a daily mean occurrence frequency of 134.67 vs. 49.32 d^{-1} during the prior- and after-monsoon-onset periods, respectively. The large contribution of CR3 observed prior to the SCS monsoon onset, coupled with its sharp decrease after the SCS monsoon onset suggests that the physical mechanisms governing its formation are

Table 1. The 1st to 4th rows show the occurrence frequency of the CRs in each month and the entire period of April-to-June, with the relative occurrence frequency (%) of each CR (occurring frequency divided by total frequency of CR1–CR6) in each month are shown in bold. The last two rows show the daily mean occurrence frequency of each CR prior to or after the SCS monsoon onset, respectively. Numbers in italics highlight the large proportion of CR3 in April and May, and CR5 in June.

	CR1	CR2	CR3	CR4	CR5	CR6	All CRs
April	906	430	3859	2699	2861	305	11060
	8.19	**3.89**	*34.89*	**24.40**	**25.87**	**2.76**	
May	1742	678	3999	2123	3131	411	12084
	14.42	**5.61**	*33.09*	**17.57**	**25.91**	**3.40**	
June	2525	998	750	802	4704	849	10628
	23.76	**9.39**	**7.06**	**7.55**	*44.26*	**7.99**	
Total	5173	2106	8608	5624	10696	1565	33772
Prior onset	33.67	17.42	134.67	70.71	99.20	12.69	364.96
After onset	84.83	32.10	49.32	44.68	131.51	22.88	365.32

quite different from those of strong convection (CR5 and CR6). The weak convective cloud mixture (CR4) also occurs more often prior to the SCS monsoon onset but makes less of a contribution to the total CR occurrence frequency than CR3.

All of the other four types of CRs (CR1–2, CR5–6) occur more often as the season advances. In particular, the daily mean occurrence frequencies of the strong convective CR and the extreme, deep convective CRs (i.e., CR5 and CR6) more clearly show sharp increases after the SCS monsoon onset, i.e., 99.20 vs. 131.51 d^{-1} for CR5 and 12.69 vs. 22.88 d^{-1} for CR6. Such increases are closely associated with more favorable thermodynamic conditions for convection development due to stronger southwesterly monsoonal flows after the SCS monsoon onset. The seasonal variations could also be related to the increased activities of subtropical synoptic systems such as surface fronts, low-level vortexes, and associated shear lines, which provide synoptic lifting for the warm-and-moist monsoonal flows (Chen et al., 2014; Li et al., 2020).

These prior- and after-monsoon-onset differences in the CR occurrence frequency are at least qualitatively consistent with previous statistical analyses using observations from the ground-based lightning location system and the CloudSat satellite, respectively. Specifically, the monthly variations of cloud-to-ground lightning flash frequencies over the targeted area show a peak in June, indicating the more frequent occurrence of strong convection (Zheng et al., 2016). The cloud fractions of stratocumulus and nimbostratus based on CloudSat data products significantly decrease from April to June, while those of deep convection and cirrus increase substantially (Guo and Zhou, 2015).

The CR occurrence frequencies over the five subregions for the months April–June, over the years 2016–17, are presented in Fig. 4. The two most frequently occurring CRs (CR3 and CR5) both appear more often on the land than offshore. Interestingly, CR3 has its highest frequency over the most polluted URB subregion followed by ELD, WLD, and NLD, which could be related to the larger aerosol optical depth over URB compared to its surrounding areas, especially larger than that which is observed offshore, leading to a larger population of smaller cloud droplets and larger COT over URB (de Leeuw et al., 2018). A recent study by Wei et al. (2020) consistently shows higher PM 2.5 concentrations over the URB region in spring than over its surrounding areas. The anthropogenic aerosols over the land could increase the number of cloud droplets and decreases their size (Twomey, 1977), which could lead to larger values of COT and higher cloud reflectance given the limited moisture supply before the SCS monsoon (note CR3 mostly occurs before the SCS monsoon as shown in Table 1). The modeling study of Zhang et al. (2020) consistently indicates that more anthropogenic aerosols could increase both liquid water content and droplet number in warm clouds over South China in April. Their study suggests that the optical thickness of warm clouds in polluted simulations is approximately twice that in clean simulations. Meanwhile, CR3 shows larger occurrence frequencies along the coastline compared to the offshore and northern mountain regions, suggesting possible impacts of the sea breeze on CR3 as the inland intrusion of sea breeze could favor cumulus congestus on land given the moderate humidity observed prior to monsoon onset. Different from CR3, the occurrence frequencies of CR5 are roughly comparable among the four subregions on the land (2351, 2590, 2360, and 2110 in WLD, NLD, URB, and ELD, respectively), but only 1285 over SEA. This could be related to the different diurnal cycles of convection over land and ocean, i.e., the oceanic convection usually has a peak before the sunrise in contrast to the typical afternoon peak of continental convection (Liu and Zipser, 2008; Xia et al., 2015; Zheng et al., 2016).

In contrast with CR3 and CR5, CR1 and CR2 (mainly consisting of optically thinner clouds with small COT) occur mainly offshore, over SEA, with much lower frequencies observed over land. This is especially noteworthy for CR2, which had an occurrence frequency of 407 summed over the four land subregions compared with that of 1699 over SEA. Moreover, the weak convective cloud mixture (CR4) occurs more frequently over the NLD than over the other four subregions. This could be related to the frequent subtropical synoptic systems (i.e., fronts, low-level vortexes, and shear lines) that often occur either over the NLD of

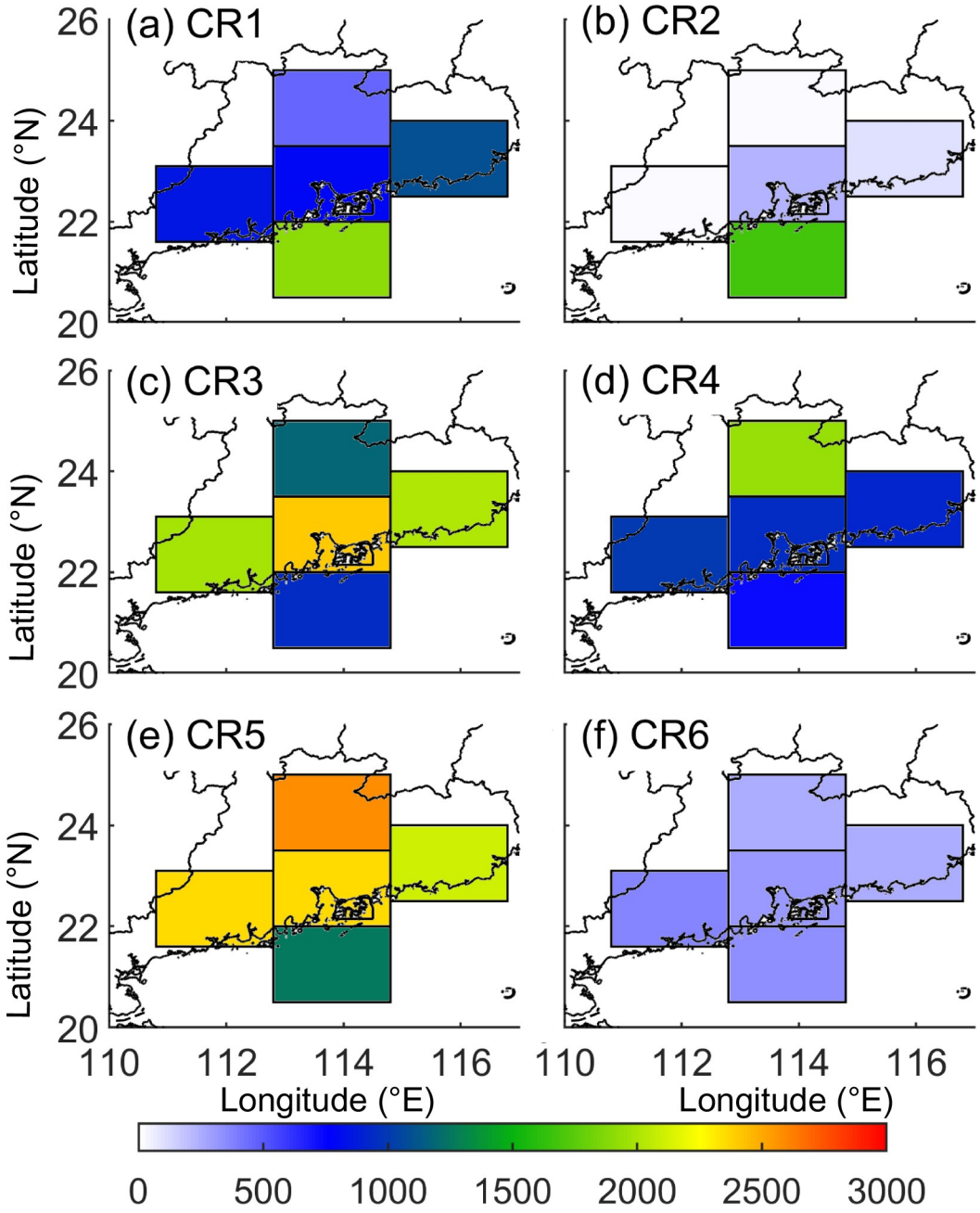

Fig. 4. Occurrence frequencies of the CRs in each subregion (i.e., WLD, NLD, URB, SEA, ELD) during the analysis period.

South China (Li et al., 2020) or in association with weather systems centered in the mid-latitudes. However, the extreme, deep convection regime (CR6) shows fewer occurrences over NLD which is closely associated with the spatial features of favorable synoptic backgrounds of this CR to be discussed in the next section.

In short summary, the occurrence of CRs exhibits substantial seasonal variation and land-sea contrast. The optically thinner cloud regimes (CR1 and CR2), strong convective cloud regime (CR5) and extreme, deep convective cloud regime (CR6) occur more frequently after the SCS monsoon onset. In contrast, the optically thick warm clouds (CR3) and weak convective clouds mixture (CR4) occur more frequently before the SCS monsoon onset. The two major types of CRs the with highest occurrence frequencies (CR3 and CR5) are most frequently found over the land, while the optically thinner CR1 and CR2 take place more often offshore. Most especially, the optically thick warm clouds (CR3) have the largest occurrence frequency over the URB compared to the other four subregions, which could be related to the higher aerosol concentrations typically present over URB.

3.3. *Rainfall characteristics of CRs*

Using the 10-min AWS rainfall records, the total rainfall amount produced by each CR on land during the study period is presented in Fig. 5. Here, the 10-min rainfall accumulation in a subregion corresponds to the cloud element observed at the end of the 10-min over the subregion. Characterized by optically thin clouds, CR1 and CR2 unsurprisingly produce little rainfall (Figs. 5a–b). With a majority of optically thick and warm clouds, CR3 can produce a small amount of rainfall, mostly over the URB subregion, and contributes only 5.66% to the total rainfall amount over the five subregions. The weak convective cloud mixture (CR4) produces 13.13% of the total rainfall amount over the five subregions with the rainfall distributed along the coastline and over NLD, noting the maximum rainfall center of about 253 mm located on the windward slope of the mountains in the southeastern portion of NLD.

The majority of rainfall amounts are produced by the

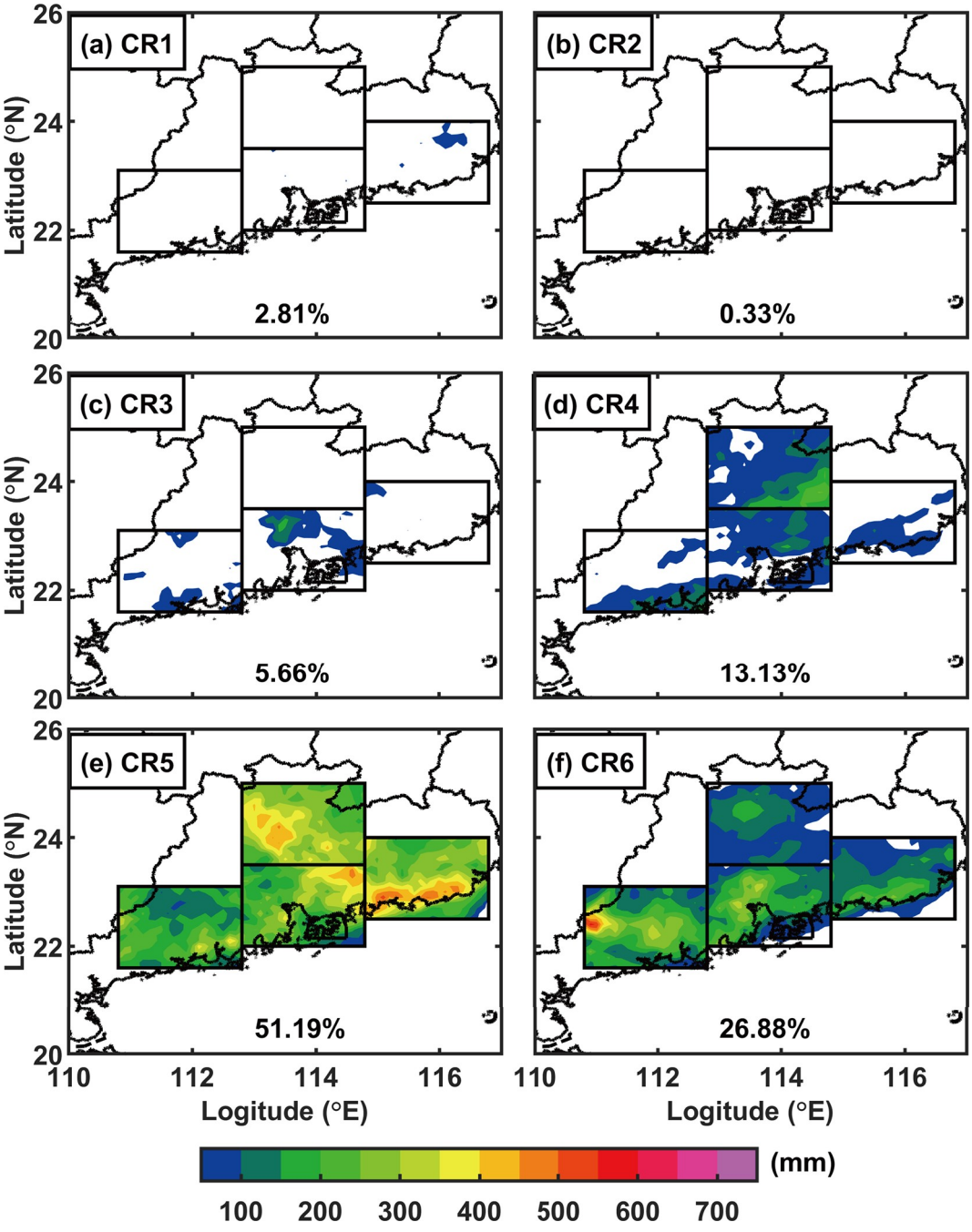

Fig. 5. Horizontal distribution of accumulated rainfall amount (mm; shading) produced by each CR during the analysis period. The contribution (%) of each CR to the total daytime-rainfall amount is labeled at the mid-lower portion of each panel. Black boxes mark the four subregions over land (i.e., WLD, NLD, URB, ELD).

strong convective clouds (CR5) and the extreme, deep convective clouds (CR6), contributing 51.19% and 26.88% to the total rainfall amount during the analysis period with the local maximum of 529 mm and 574 mm, respectively. Despite the much lower occurrence frequency of CR6, its rainfall rate is the highest among the CRs, which is consistent with its large area of optically thick clouds with the coldest cloud tops. It is evident that the highest rainfall amount produced by CR6 is located on the west side of WLD where a large number of MCSs originating from southern Guangxi province often pass through (Chen, 2018). This rainfall center has recently been found to be a center of extreme persistent heavy rainfall (Zhang et al., 2021). The rainfall center is located near a mountain (Fig. 1a), suggesting that the blocking and lifting effects from terrain contribute to the heavy rainfall production there (Zhang et al., 2021). Meanwhile, CR6-produced precipitation is also concentrated over URB and along the coastline in ELD. Different from the CR6-produced rainfall distribution, CR5 produces a larger amount of rainfall over NLD, URB, and ELD compared to WLD with the maxima located in the western NLD, northeastern URB, and along the coastline in ELD. The rainfall maximum at the windward mountains (i.e., NLD) is closely associated with the sea breeze and solar heating effects with an afternoon peak (Chen et al., 2015, 2018). The rainfall along the coast mainly initiates in the early morning as a consequence of low-level convergence between the nocturnal land breeze and onshore monsoonal winds and tends to propagate inland with the weakening of land breeze and the development of sea breeze in the daytime (Chen et al., 2015, 2016, 2018). The 91.20% rainfall contribution from CR4–CR6 obtained here is roughly consistent with Wu and Chen (2021) for the broader Asian monsoon region using the ISCCP cloud regime products. They found that the deep convection and the convective cirrus regimes contribute 80%–90% of the warm-season (April–September) rainfall.

3.4. *Synoptic Flow Patterns*

3.4.1. *General features of the SPs*

Major features of the nine SPs objectively obtained using the PCT method can be found in Fig. 6. Among these SPs, four (SP1, SP2, SP7, and SP8) are characterized by a low-pressure system located to the northwest of the targeted area with different intensities. Both SP1 and SP2 show strong 925-hPa southwesterly winds over the upstream offshore area that decelerate over coastal South China. However, compared to SP1, the high wind speeds cover a wider area over the northern SCS with a stronger southerly component in SP2, in association with larger low-pressure anomalies over South China (–30 gpm vs. –20 gpm). Under SP7 and SP8, the targeted area is influenced by weak southerly flows at the western edge of the western North Pacific subtropical high (WNPSH), while stronger winds with a southerly component are located north of the Taiwan Strait and Guangxi, respectively, in SP7 and SP8.

The other three SPs (SP3, SP6, and SP9) are characterized by a high-pressure system over the northwest land region with northerly flows approaching the northern boundary of Guangdong under SP3 and SP9, but prevailing over Guangdong under SP6. Meanwhile, marine BL southerly flows reach the coasts of Guangdong under SP3 and converge with the northerly flows. In contrast, calm winds and northeasterly winds are found offshore of South China under SP9 and SP6, respectively, indicating a lack of moisture supply from the tropical ocean to the targeted area.

The remaining two SPs (SP4 and SP5) are characterized by a high-pressure system located to the northeast and east of the targeted area, respectively. Accordingly, easterly and southeasterly flows dominate the coastal area of Guangdong and adjacent offshore areas.

3.4.2. *Major SPs associated with CR3, CR5, and CR6*

Remember that CR3 (optically thick warm clouds) has the highest occurrence frequency before the SCS monsoon onset and a strong ability to reflect shortwave radiation, while CR5 (strong convective clouds; with the highest occurrence frequency among the CRs averaged during April–June) and CR6 (extreme, deep convective clouds with the highest rain rate) collectively produce about 78% of the daytime rainfall over the four subregions on land. To examine the major SPs that favor the occurrences of the three high-impact CRs, the percentage of each CR that occurs under the nine SPs is calculated as the number of a certain CR occurring under each SP divided by the total number of this CR under all SPs. The results are displayed in Fig. 7. Note that the sum of the numbers within a column in Fig. 7 is 100%. It is shown that CR3 occurs most frequently (about one-third of CR3) under SP8, while both CR5 and CR6 (about 40% and a 50%, respectively) under SP2. In addition, about 25% of the occurrences of CR6 take place under SP3. Therefore, the thermodynamic and dynamic conditions over the targeted area under the SP2, SP3, and SP8 are further discussed in detail.

The SP2 shows strong southwesterly BL flows (about 10 m s^{-1} at 925 hPa), i.e., a low-level jet (LLJ) between the low-pressure system to the northwest and the WNPSH, transporting abundant warm and moist air to both the coastal and inland areas of South China (Fig. 8a). As a result, the targeted area is humid as evidenced by the 925-hPa relative humidity (RH) > 90% and water vapor mixing ratio reaching 16–18 g kg^{-1}. Surface winds converge along the southern coasts due to wind speed deceleration, while the 925 hPa convergence is located north of the five subregions. Both the 925 hPa temperature and 500 hPa GPH show weak gradients with mid-level horizontal winds of about 15 m s^{-1} (Fig. 8b). The temperature at the surface and 925 hPa under SP2 is the highest among the three SPs, which is not necessarily surprising as SP2 occurs mostly after the SCS monsoon onset. Altogether, this evidence suggests that under SP2, CR5 and CR6 develop in the warm sector of the subtropical shear line, with favorable thermodynamic conditions and dynamic lifting associated with the deceleration of tropical originated LLJs.

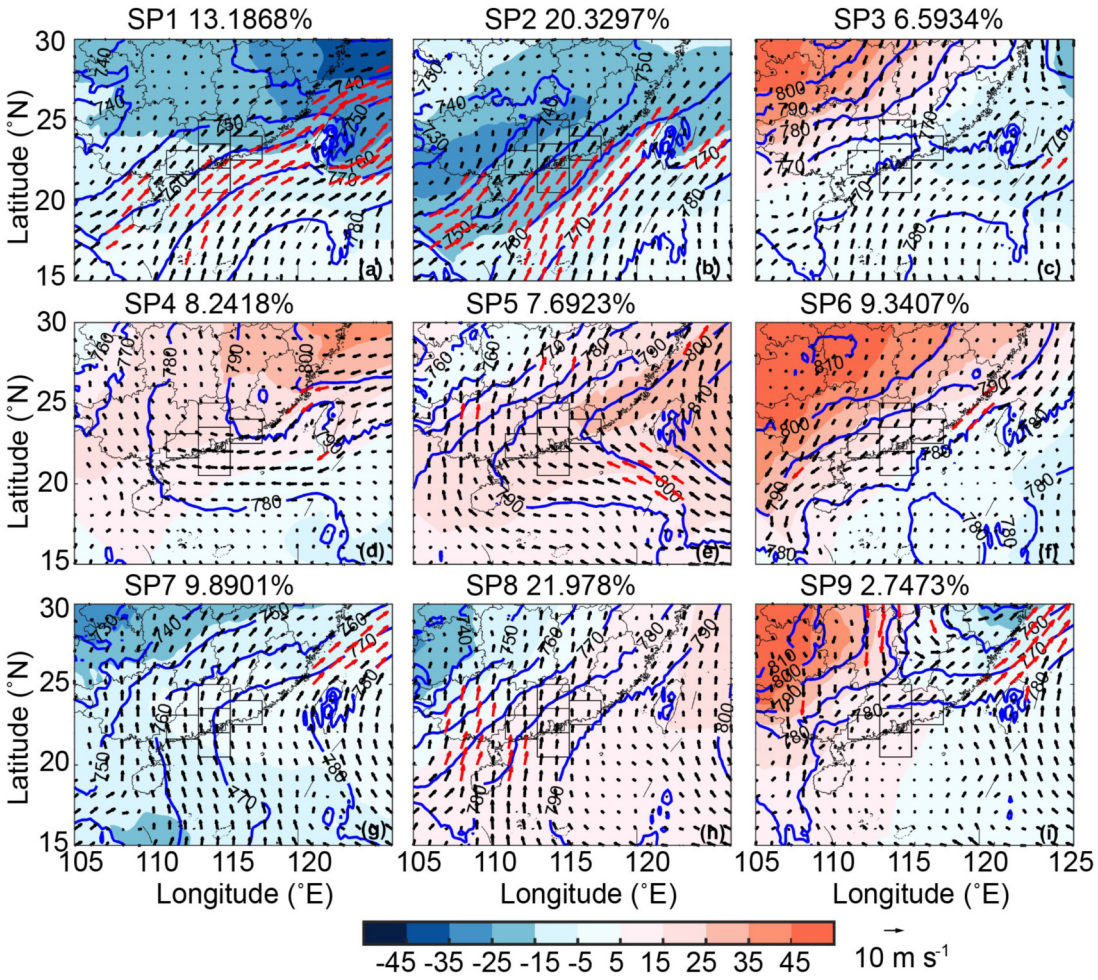

Fig. 6. The nine synoptic flow patterns objectively identified for the study period. Blue contours and arrows indicate the GPH (gpm) and horizontal winds at 925 hPa. Wind speeds greater than 8 m s^{-1} are indicated in red. Shadings represent the GPH anomaly (gpm) to the sample mean 925 hPa GPH.

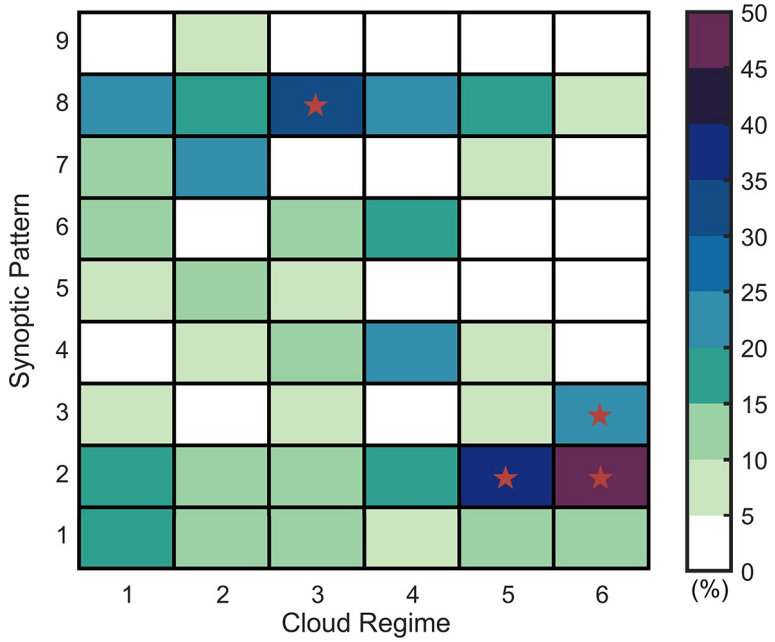

Fig. 7. Percentage (colors) of the CRs that occur under each SP. Stars in Fig.7 mark the selected SPs for CR3, CR5 and CR6.

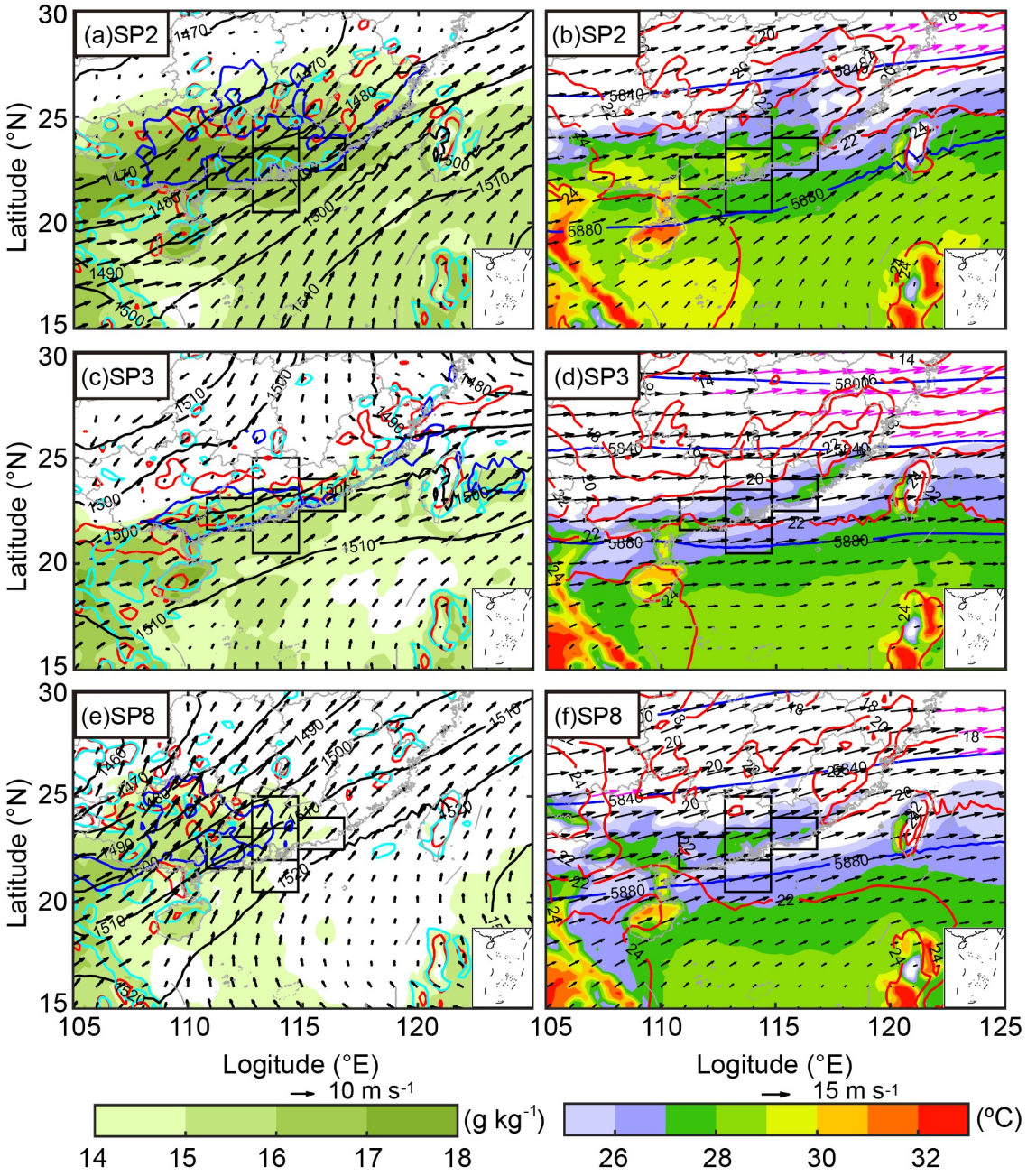

Fig. 8. Meteorological fields under the SP2, SP3, and SP8. (a), (c), and (e) The 925 hPa water vapor mixing ratio (shading), relative humidity (>90%; blue contour). Red and cyan contours indicate the wind convergence (2×10^{-5} s^{-1}) at 925 hPa and the surface, respectively. Black contour and black vectors indicate the GPH and horizontal winds at 850 hPa, respectively. (b), (d), and (f) 2-m temperature (shading), 925 hPa temperature (°C; red contour), 500 hPa GPH (gpm; black contour), and horizontal wind (vectors; wind speed greater than 15 m s^{-1} are indicated with magenta). A reference vector of 10 m s^{-1} and 15 m s^{-1}, respectively, is indicated with a black arrow above the color bar at left- and right-bottom. Black boxes mark the five subregions (i.e., WLD, NLD, URB, SEA, ELD).

Accompanied by a high-pressure center to the northwest of the targeted area under SP3, the 925-hPa northerly flows from inland areas converge with the oceanic southwesterly moist flows near the coastline, which is collocated with the surface convergence zone. The convergence at the surface and in the BL along the coastline would promote moisture accumulation and favor convection initiation (Fig. 8c), which is consistent with the concentrated rainfall produced by CR6 along the coast (Fig. 5f) and also partially explains the reduced occurrence of CR6 in the NLD subregion. The 925-hPa temperature field shows large gradients (Fig. 8d) as cold air masses are brought by the extensive northerly winds from the higher latitudes.

Under SP8, the WNPSH extends more westward, and

the moist air and convergence zone are mainly located to the west of our targeted area. Moisture amounts within the five subregions are moderate (q_v of 14–15 g kg^{-1} at 925 hPa) but are much lower compared to those under the SP2. Controlled by the WNPSH, the atmosphere over northern SCS is drier than under SP2 and SP3 (Fig. 8e) and the targeted area, for the most part, lacks low-level wind convergence.

To examine the local conditions over the targeted area under the three SPs, the joint probability density functions of CAPE-CIN, PW-vertical velocity (ω), and CAPE-ω (Fig. 9) are calculated using the grid points of ERA5 within the five subregions. Consistent with the circulation pattern discussed above, SP2 presents the largest mean CAPE because of the higher 2-m temperature (T_{2m}) and abundant moisture supply. Compared to those under SP2, the mean CAPE under SP3 is smaller as the T_{2m} is lower and the inland area is relatively dry. Of note is that the CIN under SP3 is the smallest, suggesting that the air parcels can more easily overcome the negative buoyancy when lifted by the wind convergence mechanism. Recall that SP3 also provides favorable dynamic lifting at the surface and within the BL. Compared with SP2 and SP3, reduced moisture and larger CIN, on average under SP8, make it more difficult to trigger and develop rainstorms, despite the wide range of CAPE. Although some large CAPE values exist in SP8, these large CAPE values often occur in the presence of weak vertical motion (mostly around zero in Fig. 9i) compared to SP2 and SP3. This explains the lower cloud tops of CR3, which has a

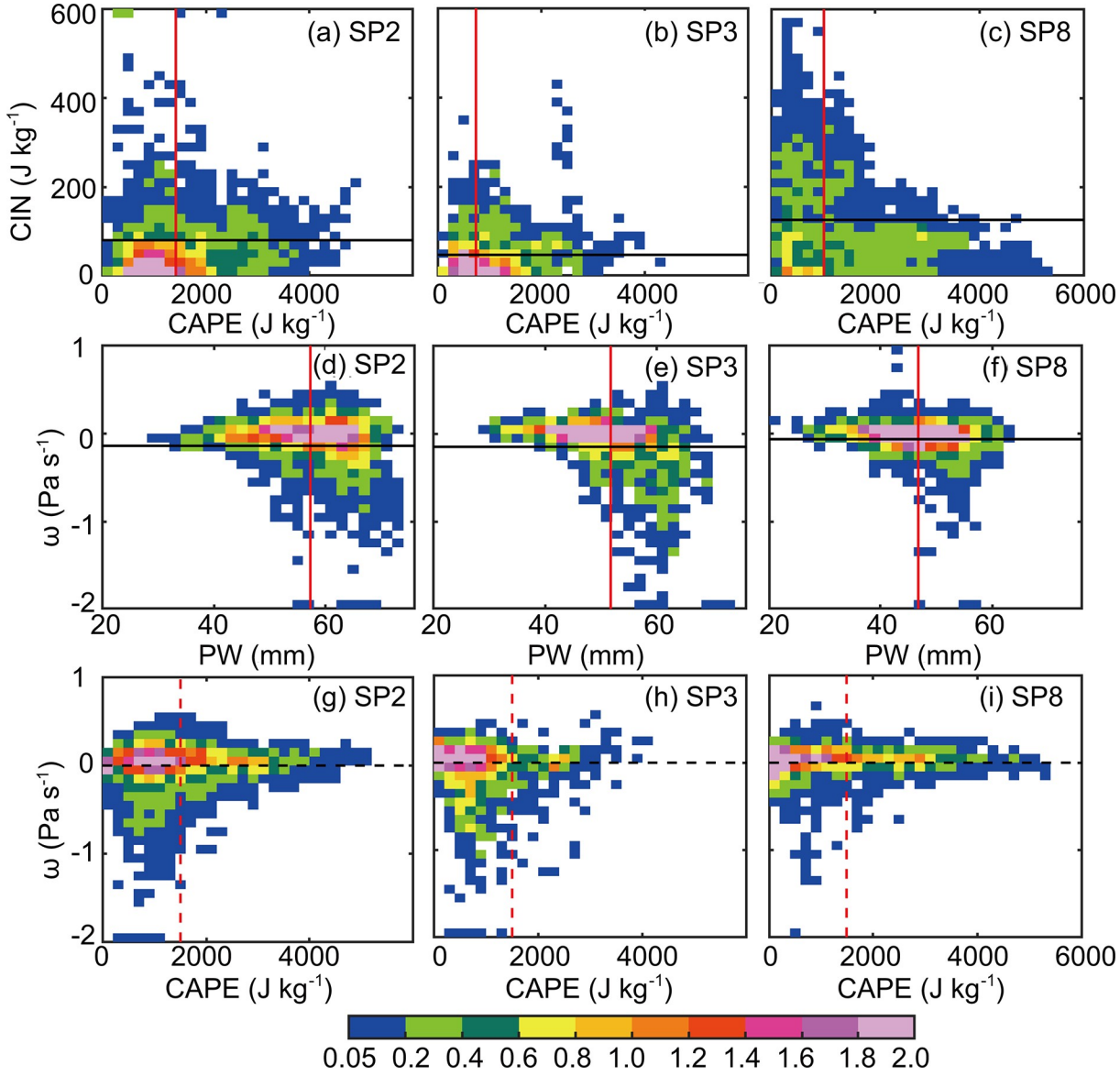

Fig. 9. Joint probability density function (shaded) of CIN-CAPE (a–c) ω-PW and (g–i) ω-CAPE (d–f) over the targeted area under SP2 (a, d, g), SP3 (b, e, h), and SP8 (c, f, i). Black and red solid lines, respectively, denote the mean values of (a–c) CIN and CAPE, and (d–f) ω and PW. Black and red dashed lines in (g–i) donate the zero line of ω and 1500 J kg^{-1} of CAPE, respectively. The means are significantly different between each pair of the synoptic patterns at the 95% confidence level, except for ω between SP2 and SP3.

mean TBB of about 11°C. The large-scale upward motions over the targeted area under SP2 and SP3 also have larger values than those under SP8. The larger PW and stronger upward motion under SP2 and SP3 indicate more favorable local environments for convective development than those under SP8.

The above analysis shows that SP2 and SP3 provide more favorable conditions for the development of strong-to-extreme convective clouds (CR5 and CR6), while SP8 can promote the formation of optically thick non-convective clouds (CR3). Having the highest water vapor transport to the coastline and inland in the boundary layer, SP2 provides the largest CAPE and PW for convective clouds to develop over the targeted area. SP3 supports moisture accumulation and strong wind convergence, mainly along the coastline, which can trigger and promote coastal convection. SP8 features moderate moisture and a wide range of CAPE over the targeted area, but with large CIN and without prominent larger-scale lifting.

4. Summary and Conclusions

Little is known about cloud regimes (CRs) in South China despite their importance to the hydrological cycle and radiation transfer over this monsoon coastal region. Using the 2 km-and-10 min observations from the AHI onboard the HW8 satellite and the FYGAT-I science product algorithm, this study identifies the CRs over coastal South China during the pre-summer rainy season (April–June) of 2016–17 based on the joint frequency distribution of TBB and COT. The CR identification and relevant properties including, cloud fraction, cloud phase, occurrence frequency, and rainfall contribution have been analyzed for five, 1.5° × 2° subregions over the targeted area. Favorable SPs for the two major rain-producing CRs and the CR with both high reflectance and high occurrence frequency are objectively identified. The main findings are as follows:

(1) Six CRs (CR1–CR6) are identified, namely, the optically thin-to-moderate cloud mixture, optically thin warm clouds with cirrus, optically thick warm clouds, weak convective cloud mixture, strong convective clouds, and extreme, deep convective clouds. CR1 consists mainly of cirrus, water, and thick ice. CR2 is mainly composed of water clouds and some cirrus. CR3 is mostly composed of water clouds. CR4–CR6 consist of increasing thick ice and decreasing overlapping cloud pixels, with CR4 having the most water and supercooled cloud pixels. CR2 is the most scattered among the CRs with median cloud fractions of 70% over each subregion. CR1 and CR3 are nearly overcast with a median cloud fraction of 90%. CR4–CR6 have convective clouds are mostly overcast with cloud fractions nearly 100%.

(2) These CRs have obvious monthly and spatial variations with clear contrasts between the prior- and after-monsoon-onset periods and also between the land and nearby offshore areas. The occurrence frequency of the optically thick warm clouds (CR3) and the weak convective cloud mixture (CR4) decrease from April to June, while those of the other four CRs increase after the SCS monsoon onset. CR3 has large reflectance and the highest occurrence frequency in April and May. It occurs more frequently over the land, especially over the urban agglomeration rather than the sea surface, which may be related to the larger anthropogenic aerosol concentrations over the cities. In contrast, CR1 and CR2 with optically thinner clouds, occur mainly offshore. Among all the CRs, the strong and extreme deep convective clouds (CR5 and CR6) produce about 78% of surface rainfall over the land subregions.

(3) Two SPs are found to be closely associated with CR5 and CR6. One is characterized by a large moisture supply along with the presence of low-level jets after the SCS monsoon onset. The other is characterized by a "northwest high-southeast low" pattern in the lower troposphere and provides strong convergence promoting convective development along the coastline. In contrast, CR3 is closely related to a SP that occurs mainly before the SCS monsoon onset, with the WNPSH extending more westward leading to a moderate amount of moisture, but large CIN and lack of synoptic lifting over the targeted area.

This study objectively identifies cloud regimes and documents their characteristics and the associated synoptic flow patterns over the densely populated area of coastal South China during the pre-summer rainy season using newly available satellite observations of 2 km-and-10 min resolutions. The findings presented herein complement previous studies that mostly focused on broader areas with a coarse resolution or heavy rain-producing convective systems over coastal South China, and thus add to our knowledge of cloud and precipitation in this region.

Acknowledgements. This work was supported by Guangdong Major Project of Basic and Applied Basic Research (Grant No. 2020B0301030004), National Natural Science Foundation of China (Grant Nos. 41775050, 42030610, 41775002, 42005008 and 41975031), and the Basic Research Fund of the Chinese Academy of Meteorological Sciences (Grant No. 2020Z010). We appreciate two anonymous reviewers for providing useful comments. The authors appreciate the Himawari-8 data shared by the Meteorological Satellite Center of Japanese Meteorological Administration, which are available via http://www.eorc.jaxa.jp/ptree/index.html. The authors also acknowledge ECMWF for providing the ERA5 Reanalysis data via https://cds.climate.copernicus.eu/cdsapp#!/home. This research is a part of the southern China Monsoon Rainfall Experiment (SCMREX), which is a Research and Development Project of the World Weather Research Programme (WWRP).

Electronic supplementary material: Supplementary material is available in the online version of this article at https://doi.org/10.1007/s00376-021-1148-1.

REFERENCES

Anderberg, M. R., 1973: *Cluster Analysis for Applications: A vol-*

ume in Probability and Mathematical Statistics: A Series of Monographs and Textbooks. *Academic Press*, 359 pp.

Bessho, K., and Coauthors, 2016: An introduction to Himawari-8 /9— Japan's new-generation geostationary meteorological satellites. *J. Meteor. Soc. Japan*, **94**, 151–183, https://doi.org/10.2151/jmsj.2016-009.

Chen, D. D., and Coauthors, 2019: Mesoscale convective systems in the Asian monsoon region from advanced himawari imager: Algorithms and preliminary results. *J. Geophys. Res.*, **124**, 2210–2234, https://doi.org/10.1029/2018JD029707.

Chen, G. X., R. Y. Lan, W. X. Zeng, H. Pan, and W. B. Li, 2018: Diurnal variations of rainfall in surface and satellite observations at the monsoon coast (South China). *J. Climate*, **31**, 1703–1724, https://doi.org/10.1175/JCLI-D-17-0373.1.

Chen, X. C., K. Zhao, and M. Xue, 2014: Spatial and temporal characteristics of warm season convection over Pearl River Delta region, China, based on 3 years of operational radar data. *J. Geophys. Res.*, **119**, 12447–12465, https://doi.org/10.1002/2014JD021965.

Chen, X. C., K. Zhao, M. Xue, B. W. Zhou, X. X. Huang, and W. X. Xu, 2015: Radar-observed diurnal cycle and propagation of convection over the Pearl River Delta during Mei-Yu season. *J. Geophys. Res.*, **120**, 12557–12575, https://doi.org/10.1002/2015JD023872.

Chen, X. C., F. Q. Zhang, and K. Zhao, 2016: Diurnal variations of the land–sea breeze and its related precipitation over South China. *J. Atmos. Sci.*, **73**, 4793–4815, https://doi.org/10.1175/JAS-D-16-0106.1.

Chen, Y. R. X., 2018: Multiple-scale characteristics of the extreme rainfall over south China during the presummer rainy season: Statistic analysis and a case study. PhD dissertation, Chinese Academy of Meteorological Sciences, 147 pp. (in Chinese with English abstract)

de Leeuw, G., and Coauthors, 2018: Two decades of satellite observations of AOD over mainland China using ATSR-2, AATSR and MODIS/Terra: Data set evaluation and large-scale patterns. *Atmospheric Chemistry and Physics*, **18**, 1573–1592, https://doi.org/10.5194/acp-18-1573-2018.

Ding, Y. H., 1994: *Monsoons Over China*. *Kluwer Acad*, 419pp.

Du, Y., and G. X. Chen, 2019: Heavy rainfall associated with double low-level jets over southern China. *Part II: Convection initiation. Mon. Wea. Rev.*, **147**, 543–565, https://doi.org/10.1175/MWR-D-18-0102.1.

Gordon, N. D., J. R. Norris, C. P. Weaver, and S. A. Klein, 2005: Cluster analysis of cloud regimes and characteristic dynamics of midlatitude synoptic systems in observations and a model. *J. Geophys. Res.*, **110**, D15S17, https://doi.org/10.1029/2004JD005027.

Guo, Z., and T. J. Zhou, 2015: Seasonal variation and physical properties of the cloud system over southeastern China derived from CloudSat products. *Adv. Atmos. Sci.*, **32**, 659–670, https://doi.org/10.1007/s00376-014-4070-y.

He, Z. W., Q. H. Zhang, L. Q. Bai, and Z. Y. Meng, 2017: Characteristics of mesoscale convective systems in central East China and their reliance on atmospheric circulation patterns. *International Journal of Climatology*, **37**, 3276–3290, https://doi.org/10.1002/joc.4917.

Huff, F. A., and J. L. Vogel, 1978: Urban, topographic and diurnal effects on rainfall in the St. *Louis region. J. Appl. Meteorol.*, **17**, 565–577, https://doi.org/10.1175/1520-0450(1978)017<0565:UTADEO>2.0.CO;2.

Huth, R., 1993: An example of using obliquely rotated principal components to detect circulation types over Europe. *Meteor. Z.*, **2**, 285–293, https://doi.org/10.1127/metz/2/1993/285.

Jakob, C., and G. Tselioudis, 2003: Objective identification of cloud regimes in the Tropical Western Pacific. *Geophys. Res. Lett.*, **30**, 2082, https://doi.org/10.1029/2003GL018367.

Jakob, C., and C. Schumacher, 2008: Precipitation and latent heating characteristics of the major Tropical Western Pacific cloud regimes. *J. Climate*, **21**, 4348–4364, https://doi.org/10.1175/2008JCLI2122.1.

Kummerow, C., W. Barnes, T. Kozo, J. Shiue, and J. Simpson, 1998: The tropical rainfall measuring mission (TRMM) sensor package. *J. Atmos. Oceanic Technol.*, **15**, 809–817, https://doi.org/10.1175/1520-0426(1998)015<0809:TTRMMT>2.0.CO;2.

Leinonen, J., M. D. Lebsock, L. Oreopoulos, and N. Cho, 2016: Interregional differences in MODIS-derived cloud regimes. *J. Geophys. Res.*, **121**, 11648–11665, https://doi.org/10.1002/2016JD025193.

Li, M. X., Q. H. Zhang, and F. Q. Zhang, 2016: Hail day frequency trends and associated atmospheric circulation patterns over China during 1960-2012. *J. Climate*, **29**, 7027–7044, https://doi.org/10.1175/JCLI-D-15-0500.1.

Li, M. X., Y. L. Luo, D.-L. Zhang, M. X. Chen, C. Wu, J. F. Yin, and R. Y. Ma, 2021: Analysis of a record-breaking rainfall event associated with a monsoon coastal megacity of South China using multisource data. *IEEE Trans. Geosci. Remote Sens.*, **59**, 6404–6414, https://doi.org/10.1109/TGRS.2020.3029831.

Li, Y. Y., R. C. Yu, Y. P. Xu, and X. H. Zhang, 2004: Spatial distribution and seasonal variation of cloud over China based on ISCCP data and surface observations. *J. Meteor. Soc. Japan*, **82**, 761–773, https://doi.org/10.2151/jmsj.2004.761.

Li, Z. H., Y. L. Luo, Y. Du, and J. C. L. Chan, 2020: Statistical characteristics of pre-summer rainfall over south China and associated synoptic conditions. *J. Meteor. Soc. Japan*, **98**, 213–233, https://doi.org/10.2151/jmsj.2020-012.

Liu, C. T., and E. J. Zipser, 2008: Diurnal cycles of precipitation, clouds, and lightning in the tropics from 9 years of TRMM observations. *Geophys. Res. Lett.*, **35**, L04819, https://doi.org/10.1029/2007GL032437.

Luo, Y. L., H. Wang, R. H. Zhang, W. M. Qian, and Z. Z. Luo, 2013: Comparison of rainfall characteristics and convective properties of monsoon precipitation systems over South China and the Yangtze and Huai River Basin. *J. Climate*, **26**, 110–132, https://doi.org/10.1175/JCLI-D-12-00100.1.

Luo, Y. L., and Coauthors, 2017: The southern China monsoon rainfall experiment (SCMREX). *Bull. Amer. Meteor. Soc.*, **98**, 999–1013, https://doi.org/10.1175/BAMS-D-15-00235.1.

Luo, Y. L., R. D. Xia, and J. C. L. Chan, 2020: Characteristics, physical mechanisms, and prediction of pre-summer rainfall over South China: Research progress during 2008-2019. *J. Meteor. Soc. Japan*, **98**, 19–42, https://doi.org/10.2151/jmsj.2020-002.

Min, M., and Coauthors, 2017: Developing the science product algorithm testbed for Chinese next-generation geostationary meteorological satellites: FengYun-4 series. *Journal of Meteorological Research*, **31**, 708–719, https://doi.org/10.1007/s13351-017-6161-z.

Oreopoulos, L., N. Cho, D. Lee, S. Kato, and G. J. Huffman, 2014: An examination of the nature of global MODIS cloud

regimes. *J. Geophys. Res.*, **119**, 8362–8383, https://doi.org/10.1002/2013JD021409.

Oreopoulos, L., N. Cho, D. Lee, and S. Kato, 2016: Radiative effects of global MODIS cloud regimes. *J. Geophys. Res.*, **121**, 2299–2317, https://doi.org/10.1002/2015JD024502.

Pavolonis, M. J., A. K. Heidinger, and T. Uttal, 2005: Daytime global cloud typing from AVHRR and VIIRS: Algorithm description, validation, and comparisons. *J. Appl. Meteorol.*, **44**, 804–826, https://doi.org/10.1175/JAM2236.1.

Poetzsch-Heffter, C., Q. Liu, E. Ruperecht, and C. Simmer, 1995: Effect of cloud types on the earth radiation budget calculated with the ISCCP Cl dataset: Methodology and initial results. *J. Climate*, **8**, 829–843, https://doi.org/10.1175/1520-0442(1995)008<0829:EOCTOT>2.0.CO;2.

Rossow, W. B., G. Tselioudis, A. Polak, and C. Jakob, 2005: Tropical climate described as a distribution of weather states indicated by distinct mesoscale cloud property mixtures. *Geophys. Res. Lett.*, **32**, L21812, https://doi.org/10.1029/2005GL024584.

Stephens, G. L., 2005: Cloud feedbacks in the climate system: A critical review. *J. Climate*, **18**, 237–273, https://doi.org/10.1175/JCLI-3243.1.

Stephens, G. L., and Coauthors, 2002: The CloudSat mission and the a-train: A new dimension of space-based observations of clouds and precipitation. *Bull. Amer. Meteor. Soc.*, **83**, 1771–1790, https://doi.org/10.1175/BAMS-83-12-1771.

Stephens, G. L., and Coauthors, 2012: An update on Earth's energy balance in light of the latest global observations. *Nature Geoscience*, **5**, 691–696, https://doi.org/10.1038/ngeo1580.

Tan, J., C. Jakob, and T. P. Lane, 2013: On the identification of the large-scale properties of tropical convection using cloud regimes. *J. Climate*, **26**, 6618–6632, https://doi.org/10.1175/JCLI-D-12-00624.1.

Trenberth K. E., J. T. Fasullo, and J. Kiehl, 2009: Earth's global energy budget. *Bull. Amer. Meteor. Soc.*, **90**, 311–324, https://doi.org/10.1175/2008BAMS2634.1.

Twomey, S., 1977: The influence of pollution on the shortwave albedo of clouds. *J. Atmos. Sci.*, **34**, 1149–1152, https://doi.org/10.1175/1520-0469(1977)034<1149:TIOPOT>2.0.CO;2.

Walther, A., W. Straka, and A. K. Heidinger, 2011: ABI algorithm theoretical basis document for daytime cloud optical and microphysical properties (DCOMP), NOAA/NESDIS Center Satellite Applications and Research: Camp Springs, MD, USA; Volume 61. Available online: https://www.goesr.gov/products/ATBDs/baseline/Cloud_DCOMP_v2.0_no_color.pdf.

Wang, H., Y. L. Luo, and B. J.-D. Jou, 2014: Initiation, Maintenance, and properties of convection in an extreme rainfall event during SCMREX: Observational analysis. *J. Geophys. Res.*, **119**, 13206–13232, https://doi.org/10.1002/2014JD022339.

Wang, X., M. Min, F. Wang, J. P. Guo, B. Li, and S. H. Tang, 2019: Intercomparisons of cloud mask products among fengyun-4A, himawari-8, and MODIS. *IEEE Trans. Geosci. Remote Sens.*, **57**, 8827–8839, https://doi.org/10.1109/TGRS.2019.2923247.

Wei, J., and Coauthors, 2020: Improved 1 km resolution $PM_{2.5}$ estimates across China using enhanced space-time extremely randomized trees. *Atmospheric Chemistry and Physics*, **20**, 3273–3289, https://doi.org/10.5194/acp-20-3273-2020.

Whiteman, C. D., 2000: *Mountain Meteorology, Fundamentals and Applications*. *Oxford University Press*, 355pp.

Wu, M. W., Y. L. Luo, F. Chen, and W. K. Wong, 2019: Observed link of extreme hourly precipitation changes to urbanization over coastal South China. *J. Appl. Meteorol. Climatol.*, **58**, 1799–1819, https://doi.org/10.1175/JAMC-D-18-0284.1.

Wu, R. T., and G. X. Chen, 2021: Contrasting cloud regimes and associated rainfall over the South Asian and East Asian monsoon regions. *J. Climate*, **34**, 3663–3681, https://doi.org/10.1175/JCLI-D-20-0992.1.

Xia R. D., Zhang, D.-L., and Wang, B. L., 2015: A 6-yr cloud-to-ground lightning climatology and its relationship to rainfall over central and eastern China. *J. Appl. Meteorol. Climatol.*, **54**, 2443–2460, https://doi.org/10.1175/JAMC-D-15-0029.1.

Xu, W. X., E. J. Zipser, and C. T. Liu, 2009: Rainfall characteristics and convective properties of Mei-Yu precipitation systems over South China, Taiwan, and the South China Sea. *Part I: TRMM Observations. Mon. Wea. Rev.*, **137**, 4261–4275, https://doi.org/10.1175/2009MWR2982.1.

Yin, J. F., D.-L. Zhang, Y. L. Luo, and R. Y. Ma, 2020: On the extreme rainfall event of 7 May 2017 over the coastal city of Guangzhou. *Part I: Impacts of urbanization and orography. Mon. Wea. Rev.*, **148**, 955–979, https://doi.org/10.1175/MWR-D-19-0212.1.

Zhang, C., X. G. Huang, J. F. Fei, X. Luo, and Y. Zhou, 2021: Spatiotemporal characteristics and associated synoptic patterns of extremely persistent heavy rainfall in southern China. *J. Geophys. Res.*, **126**, e2020JD033253, https://doi.org/10.1029/2020JD033253.

Zhang, J. P., and Coauthors, 2012: The impact of circulation patterns on regional transport pathways and air quality over Beijing and its surroundings. *Atmospheric Chemistry and Physics*, **12**, 5031–5053, https://doi.org/10.5194/acp-12-5031-2012.

Zhang, L. J., and Coauthors, 2020: Anthropogenic aerosols significantly reduce mesoscale convective system occurrences and precipitation over Southern China in April. *Geophys. Res. Lett.*, **47**, e2019GL086204, https://doi.org/10.1029/2019GL086204.

Zhang, Y. Y., S. Klein, G. G. Mace, and J. Boyle, 2007: Cluster analysis of tropical clouds using CloudSat data. *Geophys. Res. Lett.*, **34**, L12813, https://doi.org/10.1029/2007GL029336.

Zhao, Y. Y., Q. H. Zhang, Y. Du, M. Jiang, and J. P. Zhang, 2013: Objective analysis of circulation extremes during the 21 July 2012 torrential rain in Beijing. *Acta Meteorologica Sinica*, **27**, 626–635, https://doi.org/10.1007/s13351-013-0507-y.

Zheng, D., Y. J. Zhang, Q. Meng, L. W. Chen, and J. R. Dan, 2016: Climatological comparison of small- and large-current cloud-to-ground lightning flashes over southern China. *J. Climate*, **29**, 2831–2848, https://doi.org/10.1175/JCLI-D-15-0386.1.